China Wildfire Emission Dataset (ChinaWED v1) for the period 2012-2022

Zhengyang Lin[a], Ling Huang[a], Hanqin Tian[b], Anping Chen[c], Xuhui Wang[a*]

a. Institute of Carbon Neutrality, Sino-French Institute of Earth System Sciences, College of Urban and Environmental Sciences, Peking University, Beijing, China
b. Center for Earth System Science and Global Sustainability, Schiller Institute for Integrated Science and Society, Department of Earth and Environmental Sciences, Boston College, Chestnut Hill, MA, USA
c. Department of Biology and Graduate Degree Program in Ecology, Colorado State University, Fort Collins, USA
**Correspondence to*: Xuhui Wang(xuhui.wang@pku.edu.cn)

Non-technical summary

We developed a country-level fire emission model with updates in burned biomass calculation and emission factors in China. We found that agricultural fires make up most of the emissions while greenhouse gas emissions from forests and grasslands fires are decreasing significantly. Fire emissions peak in late spring, with hotspots in Northeast, Southwest, and East China. Our findings provide important estimates as a part of the budget for the national terrestrial ecosystems.

Abstract

During the past decades, wildfires have undergone rapid changes while both the extent of fire activities and the resulting greenhouse gas (GHG) emissions from wildfires in China remain inadequately quantified. We established a wildfire emission model to generate the China Wildfire Emission Dataset (ChinaWED) which can therefore be used to explore the recent dynamics at national scale. This dataset is constructed at monthly and kilometer scale under a consistent and quantifiable calculation framework, providing an average annual estimates of wildfire-induced GHG emissions of 78.13 ± 22.46 Tg CO_2, 279.47 ± 82.01 Gg CH_4, and 6.26 ± 1.67 Gg N_2O for the past decade. We observed significant decreases in both wildfire occurrences and emissions within forests and grasslands. This trend, however, is counteracted by the variations of agricultural fires, which constitute the primary type accounting for at least half of the national total fire emissions. The seasonal cycle of wildfire GHG emissions show an evident apex occurring during the transition from mid-spring to early-summer. At the regional scale, Northeast, Southwest and East China emerge as hotspots for wildfire-induced emissions. Our study offers new insights into understanding China's wildfire dynamics and provides a detailed regional model for the wildfire greenhouse gas emissions over China.

1. Introduction

Wildfires exert a substantial impact on landscape vegetation while influencing the biogeochemical cycle through the emissions of greenhouse gases (GHG) (Bauters et al., 2021; Guo et al., 2024; Rodríguez Vásquez et al., 2021). Approximately 2.1 × 10^{15} grams (Petagrams, Pg) of carbon were emitted globally through biomass burning, representing about 22% of all fossil fuel emissions in 2021 (Friedlingstein et al., 2022; van Wees et al., 2022; van der Werf et al., 2017). It constitutes a crucial component of the global and regional GHG budget (carbon dioxide (CO_2), methane (CH_4) and nitrous oxide (N_2O)), which is of particular concern giving 120 countries have pledged to achieve net zero GHG emissions. China, in particular, announced and initiated long-term climate plans, aiming for carbon peaking by 2030 and carbon neutrality by 2060 (Liu et al., 2022). Additionally, over the past decade in China, climate-driven fire weather, expanding vegetation-based fuel loadings, and anthropogenic activities have led to rapidly changing fire dynamics (Wang et al., 2023a; Wiedinmyer et al., 2023; Ying et al., 2018). To address the challenge and achieve the goals, one key step is to establish a national scale dataset that reflects the recent wildfire emission dynamics and contributes to the domestic GHG budget (Friedlingstein et al., 2022).

Currently, there have been different studies working on the estimates of China wildfire emissions including contributions from some global products. One of the most widely-used approaches take the product of emission factors, fuel loadings, burned area and combustion efficiency as the estimate of emissions. It should be noted that the limitations stem from various aspects during the calculation steps. For example, these studies may use the universal parameters (e.g., land cover types, emission factors) that do not match with characteristics of local fuels and further estimates (van Wees et al., 2022; Wiedinmyer et al., 2023). Uncertainty also arises from estimates of burned area due to the remote sensing-based fire datasets with different emphasis (e.g., active fire product and burned area product) (Chen et al., 2020; Giglio et al., 2018; Schroeder et al., 2014). Some other research focused on agricultural fire emissions adopted traditional "crop-yield-based approaches" (CYBAs), primarily relying on provincial statistical data and field-reported measurements such as crop production and estimates of burned crop residues (Hong et al., 2023; Li et al., 2016). These parts are hard to verify and can only be measured within administrative boundaries. In addition, the estimates from CYBAs typically have relatively long updating cycles, often on a yearly scale. These approaches form the fundamental framework of emission estimates, yet various input parameters were incorporated and the emissions of GHGs may not be consistent even within products.

Here, we present the China Wildfire Emission Dataset (ChinaWED v1) for the period from 2012 to 2022 at monthly and kilometer scale. We focused on the limitations existing in current studies and products and refined the estimates of calculation components. Emission factors that are specifically suited for evaluating wildfire emission in China retrieved from previous studies conducted domestically and in neighboring countries were collected. Previous studies have reported a majority of wildfire occurrences in croplands, highlighting the need for improved burned area estimates that incorporate small-size fire activities (Ying et al., 2021; Zhang et al., 2015). The newly developed product is easily to update with only one-month to two-months lag and provide consistent results for all three GHGs under same calculation framework. With the support of this ChinaWED product, we can also capture and explore the magnitude, patterns, trends and drivers of the wildfire occurrences and the wildfire-induced emissions in China within the past decade.

2. Methods

2.1 Emission estimation

In this study, we adopted the wildfire emissions estimation method based on the combination of four components: burned area, fuel load, emission factor and combustion completeness, calculated by the following equation:

$$E_{i,x,t} = \sum_{j}^{n} BA_{t,x} \times FL_x \times EF_{i,j} \times CC_{x,j} \tag{1}$$

where the subscript i represents specific emission types, j represents different vegetated cover types, x and t stand for spatial and temporal information; $E_{i,x,t}$ is hence the estimated amount of emission type i in location x and month t; $BA_{t,x}$ is the total aggregated burned area derived from multisource of satellite-based products in location x and month t; FL_x is fuel load in location x; $EF_{i,j}$ is emission factor of specific emission type i for vegetated cover type j; $CC_{x,j}$ is defined as combustion completeness in location x for vegetated cover type j.

2.2 Burned area calculation

Satellite-based thermal anomalies include burned area and active fire products, equipping researchers with the capability to observe these distinctive signatures across extensive spatial and temporal ranges. Burned areas are determined by analyzing the disparities in visible and near-infrared channels between pre- and post-fire satellite images. One of the most common limitations in burned area products is the exclusion of small-sized or smoldering fires. In contrast, active fire detection is capable of sensing these fires benefitting from the use of the thermal-sensitive mid-infrared channel. Here we use MODIS burned area product and achieved FIRMS VIIRS S-NPP active fire records as the main input datasets (Giglio et al., 2018; Schroeder et al., 2014).

MCD64A1 provides burned area classification at 500 m spatial resolution and monthly temporal resolution. VIIRS S-NPP provides daily active fire detection at 375 m spatial resolution. Given active fire detection's capability to identify fires occupying 5% or less of a pixel, the S-NPP active fire records can provide more detailed information, particularly in regions like China where numerous crop residue burnings occur. Current models and studies counted the active fire points located outside existed burned area directly as the supplementary sources for the fire activities. To avoid the potential excessive measurement, a reanalysis system combining both burned area and active fire was designed and demonstrated in Fig S1. We reconstructed the external burned area derived with circular kernels centered at those active fire records. The aggregated burned area is calculated as below:

$$BA_{t,x} = BA_{main(t,x)} + \sum_{m}^{n} AF_{sf(t,x,m)} \qquad (2)$$

where the subscript and left part of the equation is same with that in equation (1); $BA_{main(t,x)}$ represents the burned area cells in location x and month t; the sum of $AF_{sf(t,x,m)}$ represents potential burned area determined through the counting of decomposed small pixels from circular kernels centered at those active fire records (Fig. S1 and Fig. S2).

Additionally, we incorporated an independent inventory of fixed-location heat sources. This inventory is featured by continuously operating heat-source objects and spatiotemporal-aggregation characteristics in thermal anomalies. It encompasses heat-source objects including active volcanos, industrial heat sources (e.g., coal-related plants, nonmental mineral producing, ferrous metal related plants) (Liu et al., 2018). We utilized this inventory as a filter to exclude false active fire detection pixels that are not caused by wildfires. Finally, the processed burned area results were resampled to 1 km spatial resolution to match the fuel load and land cover mapping. In general, nearly three quarters (76.2%) of the total burned area is derived directly from the MCD64 burned area product, while 24.5% is supplemented by information from VIIRS S-NPP 375 m active fire records Through the incorporation of an independent fixed heat source dataset, we were able to filter out 0.7% of the burned area.

2.3 Calculation of other components

Prior studies integrated upscaled systematic field investigations and regional or national censuses to map the fuel load. Recent results showed that AGB can serve as a proxy observation, enabling indirect estimations of dry matter. Remotely sensed biomass carbon density maps aiming at limited vegetation types have been widely used. Here we used the newly developed 300 m spatial resolution dataset from Spawn et al. that incorporates multisource previously presented biomass map and harmonizes AGB from different vegetation types (Noon et al., 2022; Spawn et al., 2020).

We used land cover product from the ESA Climate Change Initiative to describe the different vegetation types (Li et al., 2018). This product has identical spatial resolution to this harmonized AGB dataset. We further aggerated the initial 37 classes into three major vegetated categories, namely forests, herbaceous and cropland. To refine the estimation of crop residue burning, several independent datasets of high-resolution crop type mapping are utilized as well. These dataset contain spatial distribution of double season paddy rice (Pan et al., 2021), single season rice (Shen et al., 2023), maize (Shen et al., 2022), winter wheat (Dong et al., 2020) and sugarcane (Zheng et al., 2022) with 10 m or 20 m spatial resolution.

It should be noted that the resolution of all these above datasets were downscaled to 1 km. AGB was calculated by summing all pixels, land cover was determined based on the mode value of vegetated categories, and detailed crop types were identified by counting classified pixels. AGB provided consistent and seamless estimations of biomass carbon density globally for the fixed year 2010. Land cover data were computed from 2001 to 2020, while crop type mapping was primarily calculated between 2017 and 2020. We utilize annual land cover data associated with the burned area for the corresponding year (mapping the burned area in 2020 for the period from 2020 to 2022). For distinct crop types, we specifically employ the results obtained during their respective growing seasons, coupled with the monthly burned area data. The averaged multiyear crop type mapping was harmonized into land cover data where agricultural land use pixels were present.

Different previous studies applied constant thresholds which is considered a major bias in emission estimation (Zhang et al., 2008). We adopted a method based on the combination of land cover types and fraction of burned (FB) assigned as a function of tree cover (Wiedinmyer et al., 2023; Wu et al., 2018; Zhang et al., 2011). Agricultural land use was set to fixed combustion completeness value to 0.93. Herbaceous had similar high CC values defined by the fraction of tree coverage while forests had much lower CC values. The detail values are listed in Table S.1 .

Emission factors for different vegetation and emission types were summarized in Table S.2. Apart from the studies that introducing global fire emissions, we selected publications that focused on affected burned areas in China and neighboring countries. Detailed emission factors of different crop types were one of the primary objectives and used in this study to help improve our burned area-based emission estimation. Forests were divided into tropical, temperate and boreal types, identified by the updated digital Köppen–Geiger world map of climatic classification (Beck et al., 2018).

3. Results

3.1 Characteristics of China wildfires and emissions

ChinaWED was calculated based on a burned area-based approach. We integrated different remotely sensed datasets that map regions affected by wildfires and detect active fire spots to reconstruct the burned area. From 2012 to 2022, the total burned area in China amounted to 5.31 ± 1.70 million hectares per year (Mha yr^{-1}) (Fig. 1). More than four-fifths of the total burned area were located in croplands, equivalent to the land area of Switzerland. 11.0% of the burned area occurred in various types of forests, while less than 6% of the burned area took place in grasslands or other herbaceous-dominated regions. Based on this burned area estimates and calculation of other components (emission factors, fuel loads, etc. see methods), our results showed that annual wildfire-induced GHG emissions in China amounted to 78.13 ± 22.46 Teragrams (Tg) CO_2, 279.47 ± 82.01 Gigagrams (Gg) CH_4, and 6.26 ± 1.67 Gg N_2O (Fig. 1). Although the majority of all wildfire-induced GHG emissions were still caused by cropland fires, the proportions were quite different from that in burned area. A fifth of CO_2 (21.1%) and CH_4 (19.9%) emissions were caused by forest fires, which was almost double the contribution of this type measured in area. This comes from the differences in background fuel loads as measured in carbon pools between forests and cropland, reported by research on China's terrestrial ecosystems (Tang et al., 2018). An even more substantial proportion of national N_2O emissions came from forest fires, reaching 37.1% of the total(Fig. 1). Wildfire-induced N_2O emissions are highly dependent on the ratio of carbon to nitrogen in vegetation fuels, which was higher in woody areas (Vernooij et al., 2021). In comparison to wildfires on other land cover types, grassland fires played a comparatively minor role in wildfire dynamics and emissions.

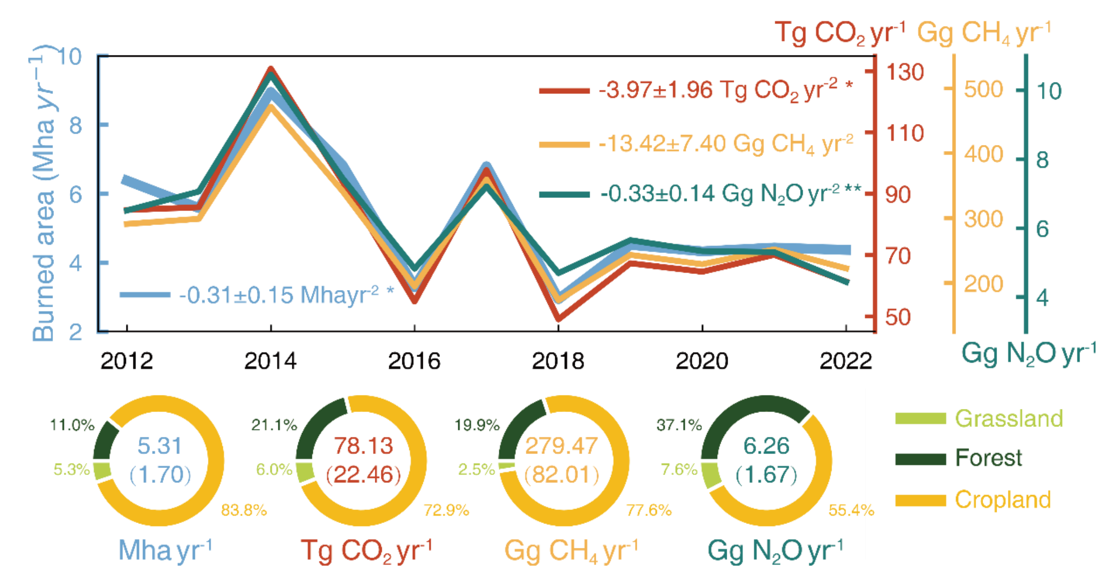

Fig. 1. The time-series and trends of China burned area and wildfire-induced emissions (CO_2, CH_4, N_2O).

The bottom pie charts demonstrate the annual averages (standard deviation within the brackets) and the proportions of different land cover types during the study period. Note that significant trends are denoted by asterisks (*P < 0.1 and **P < 0.05).

During this period, the dataset recorded a decline trend of -0.31 ± 0.15 Mha yr^{-2} (P<0.1) (Fig. 1). All vegetation wildfires decreased at different magnitudes, resulting in pervasive and slightly different declines in the three greenhouse gases. Agricultural fires had been gradually limited and demonstrated a decline in burned area at -0.26 ± 0.14 Mha yr^{-2}. Affected by the variations of agricultural fires, our dataset exhibited a statistically insignificant decline during the study period, with rates of -2.41 ± 1.81 Tg CO_2 yr^{-2}, -8.97 ± 6.96 Gg CH_4 yr^{-2} and -0.15 ± 0.11 Gg N_2O yr^{-2} during the study period. Compared with cropland, burned area and all three types of wildfire-induced greenhouse gases in forests and grasslands dropped significantly and rapidly. The decline in forest fires contributed to nearly a third (CO_2 at -1.22 ± 0.36 Tg yr^{-2}, P<0.01 and CH_4 at -3.93 ± 1.21 Gg yr^{-2}, P<0.05) and a half (N_2O at -0.15 ± 0.05 Gg yr^{-2}, P<0.05) in the total trends of emissions (Fig. S3). The grassland contributed to smaller in all these GHGs (CO_2 at -0.34 ± 0.08 Tg yr^{-2}, P<0.01, CH_4 at -0.51 ± 0.13 Gg yr^{-2}, P<0.01, and N_2O at -0.03 ± 0.01 Gg yr^{-2}, P<0.01) within the past decade.

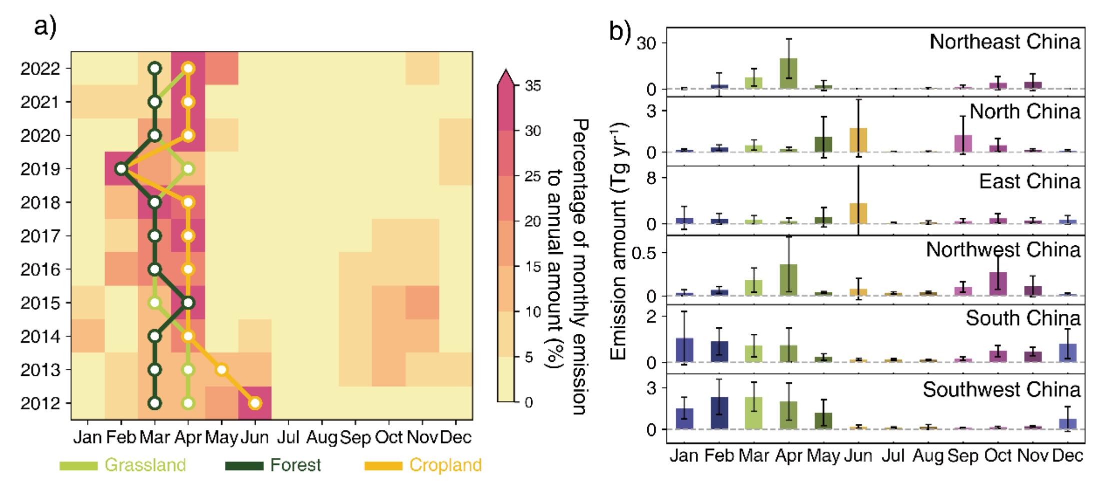

Fig. 2. Seasonal cycle of national and regional wildfire-induced CO_2 emissions.

(a) Monthly emission patterns from various land cover types: grassland (green), forest (dark green), and cropland (yellow). The data points connected by lines for different land cover types indicate the peak emission month for each year. The heatmap illustrates emission intensity (unit: arbitrary scale), with brighter colors denoting higher emission levels.

(b) Average monthly CO_2 emissions across six regions of China: Northeast China, North China, East China, Northwest China, South China, and Southwest China. Each region is plotted on distinct Y-axes to highlight seasonal variations. Four sets of colors represent the four seasons. Detailed regional divisions are introduced in Fig. S4 and their patterns in Fig. 3. Seasonal and interannual patterns for wildfire-induced CH_4 and N_2O emissions are illustrated in Fig. S5 and Fig. S6.

The outcomes derived from diverse regions and land cover types underscored those fires originating within cropland significantly dominated the overarching dynamics of national wildfires and emissions. A spatiotemporal association was assumed to exist between agricultural activities, particularly those related to planting and harvesting preparations, and the incidence of wildfires. Throughout our study period, the majority of all three types of GHG were concentrated in the first half of the year. More than half of the annual CO_2 emissions from wildfires were observed from late winter to middle spring (February to April), along with nearly the identical relative proportions of CH_4 and N_2O. A secondary seasonal peak of wildfire-induced emissions occurred in the harvest seasons in autumn (September to November), accounting for nearly 20% of the annual total (Fig. 2a). We divided six specific wildfire-induced emissions regions dependent on geographical location and environmental characteristics (Fig. S4 and Table S3). The patterns of double peaks in agricultural fire emissions in Northeast China had a significant impact on national emission levels. During the major emission season, three quarters of the region's total annual amount was emitted. It is important to note that the temporal patterns are closely associated with the local sowing and harvesting seasons (Fig. 2b) (Cheng et al., 2022; WANG et al., 2020). Similarly in North China, the major peak occurred in early summer (May and June) while the secondary peak in mid-autumn (September and October). A total of 2.75 Tg and 1.65 Tg of annual CO_2 emissions induced by agricultural fires were concentrated during these respective time periods. East China displayed disparate seasonal patterns, with the majority of agricultural fires occurring during the summer when the planting and harvest were made in double-season paddy rice fields in this area (Fig. 2b) (Pan et al., 2021; Wu et al., 2023). Approximately one-third of the annual regional emissions induced by wildfires were concentrated in June. Consequently, this correlation is validated through the examination of seasonal cycles in wildfire occurrences, which becomes a prominent temporal feature that drive the dynamics of national-scale wildfire-induced emissions (Zhang et al., 2015).

3.2 Spatiotemporal pattern of wildfire and its GHG emissions

To further explore the fire emission dynamics, we calculated the provincial and monthly burned areas and emissions, which were then aggregated to obtain regional and seasonal statistics. The results showed that the national wildfire-induced emissions shared similar patterns of all three GHG types in spite of their large disparities at both spatial and temporal scales. More than four-fifths of the total of domestic wildfire-induced GHG emissions (82.8% for CO_2, 83.2% for CH_4, and 83.6% N_2O) located in three primary peaks, the Northeast, Southwest and East China, respectively (Fig. 3), which will be introduced in detail in the upcoming sections.

In all six regions, Northeast China (Heilongjiang, Jilin, Liaoning and Nei Mongol) affected by the highest wildfire emissions. Heilongjiang and Jilin were the top two provinces not only within the region but also nationwide. Many of the burned area and emissions located in vast plains (SongNen, Liaohe and Sanjiang plain) of Northeast China. The vegetation-sourced fire emissions from these two provinces contributed to nearly one-third and one-tenth of the total domestic emissions, individually. Moreover, they exhibited a mild increasing trend compared to the national pattern, registering at non-significant trends of 0.14 ± 0.15 Mha yr^{-2} for burned area and 1.92 ± 1.92 Tg yr^{-2}, 6.94 ± 7.34 Gg yr^{-2} and 0.11 ± 0.13 Gg yr^{-2} for CO_2, CH_4 and N_2O, respectively (Fig. 4). According to data from the National Bureau of Statistics, these four provinces collectively accounted for a quarter of the sown area and grain production over the past decade. The extensive grain cultivation areas, coupled with the widespread practice of burning crop residues for land clearing, have significantly contributed to the high levels of wildfire-induced emissions associated with agricultural land use in Northeast China. CO_2 emissions from crop residue burning accounted for 82.7% of the regional total wildfire-induced emissions and 62.5% of the domestic emissions for this type. The rising trends of agricultural fires constitute the majority of regional wildfire dynamics.

Fires have been controlled to an average of 0.27 Mha of burned area per year through systematic fire and forest management in this area (Fig. 3 and Fig. 4). For comparison, a single fire event, namely the 1987 Great Black Dragon Fire, destroyed 1.33 Mha of forests and resulted in nearly two hundred fatalities (Zhao et al., 2020; Zong et al., 2022). The boreal forest wildfires led to 5.28 Tg CO_2, 19.44 Gg CH_4 and 0.94 Gg N_2O, constituting 12.3% of the total wildfire-induced emissions of this region. This amount was also equivalent for nearly ninety percent of the boreal forest wildfire emissions nationwide. Grassland fires in Northeast China, specifically in the Hulun Buir and Xilingol grasslands, attracted national attention, accounting significantly for the total amount at 67.2% for burned area and 46.7% for wildfire-induced emissions respectively.

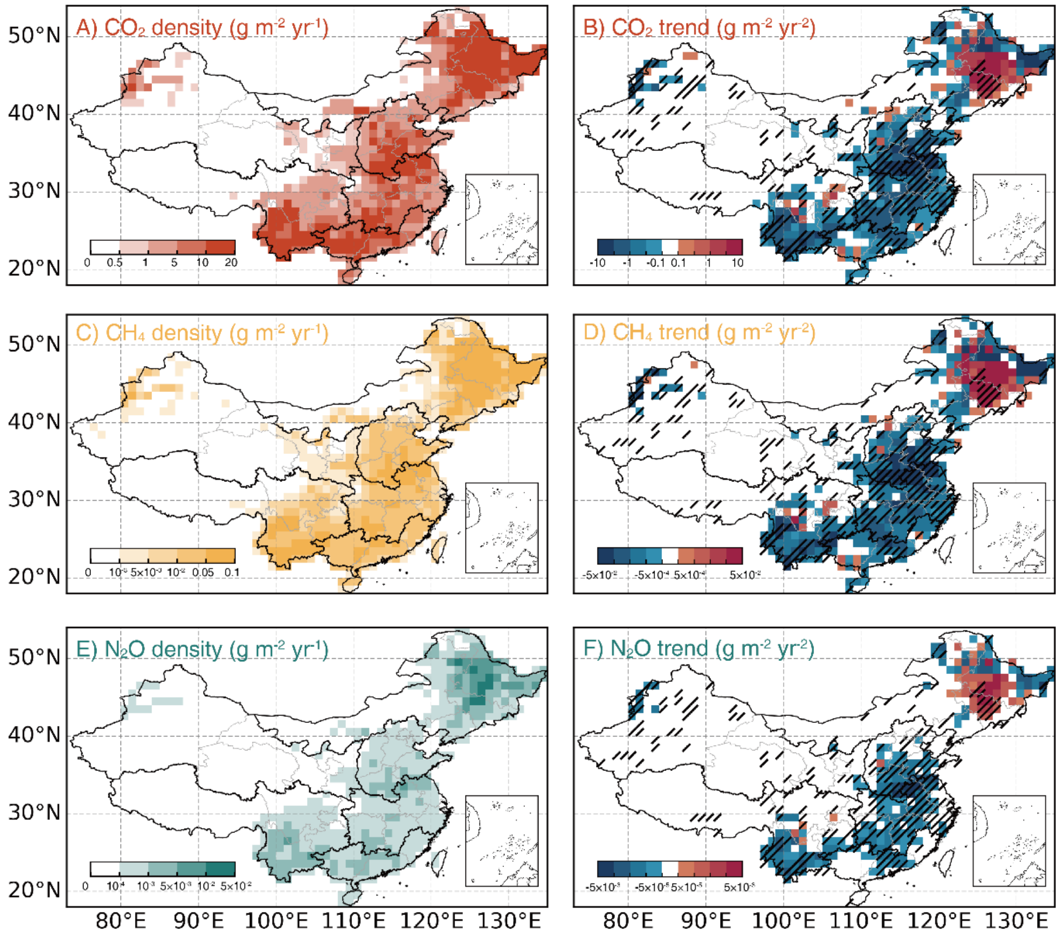

Fig. 3. Spatial distributions of the density and the trends of wildfire-induced emissions (CO_2, CH_4 and N_2O).

Subplots (a, c, e) show the density patterns and (b, d, f) for the trends. Their colors correspond to that in Fig. 1. To achieve better visual performance, the map demonstrated the density and trends in 1° grids where hatched area indicates significant trends (*P*<0.05). Locations of the provinces and regions are described in Fig. S4.

Southwest China, covering five provincial administrative areas (Yunnan, Sichuan and Guizhou provinces, Chongqing and Xizang Autonomous Region), was the second-largest regional scale emitter of fire-sourced greenhouse gases (Fig. 3). This region stands out as the only area where agricultural wildfires do not dominate; instead, temperate forest fires emitted more than all the other vegetation fires in this region (Fig. 4) (Cui et al., 2022; Ying et al., 2021). Yunnan province, a pivotal player in shaping the wildfire dynamics of this region, contributed substantially, with an annual burned area of 0.16 Mha, emitting 7.57 Tg CO_2, 23.13 Gg CH_4, and 0.81 Gg N_2O. These figures accounted for over 60% of the regional burned area and wildfire-induced emissions. From the perspective of recent trends, this province contributed to 82.4% of the regional decrease in burned area and an even larger share in the reduction of wildfire-induced emissions. The border fires showed some shared similarities in fire spreading mechanisms and environmental factors between this region and the adjoining Indo-China Peninsula, a global wildfire hotspot. However, in comparison to the rapid land cover changes and massive relevant wildfires reported in Southeast Asian countries, involving activities such as slash-and-burn, commercial forest loss, and drainage in peatlands (Curtis et al., 2018; Page et al., 2022), Southwest China had fewer and weaker fire activities related with this type. The occurrences of forest fires usually arose from occasional personal activities or fire-related cultural traditions (Ying et al., 2021). On the other hand, due to recent implementations of fire policies and long-standing efforts from firefighting teams, Southwest China has experienced a significant decline in forest fires, with a decrease of -0.02 ± 0.00 Mha yr^{-2} (P<0.01) for burned area and -0.74 ± 0.23 Tg yr^{-2} (P<0.05), -2.38 ± 0.74 Gg yr^{-2} (P<0.05) and 0.09 ± 0.02 Gg yr^{-2} (P<0.05) for CO_2, CH_4 and N_2O, respectively. This reduction accounts for more than 65% of national declines in forest fires.

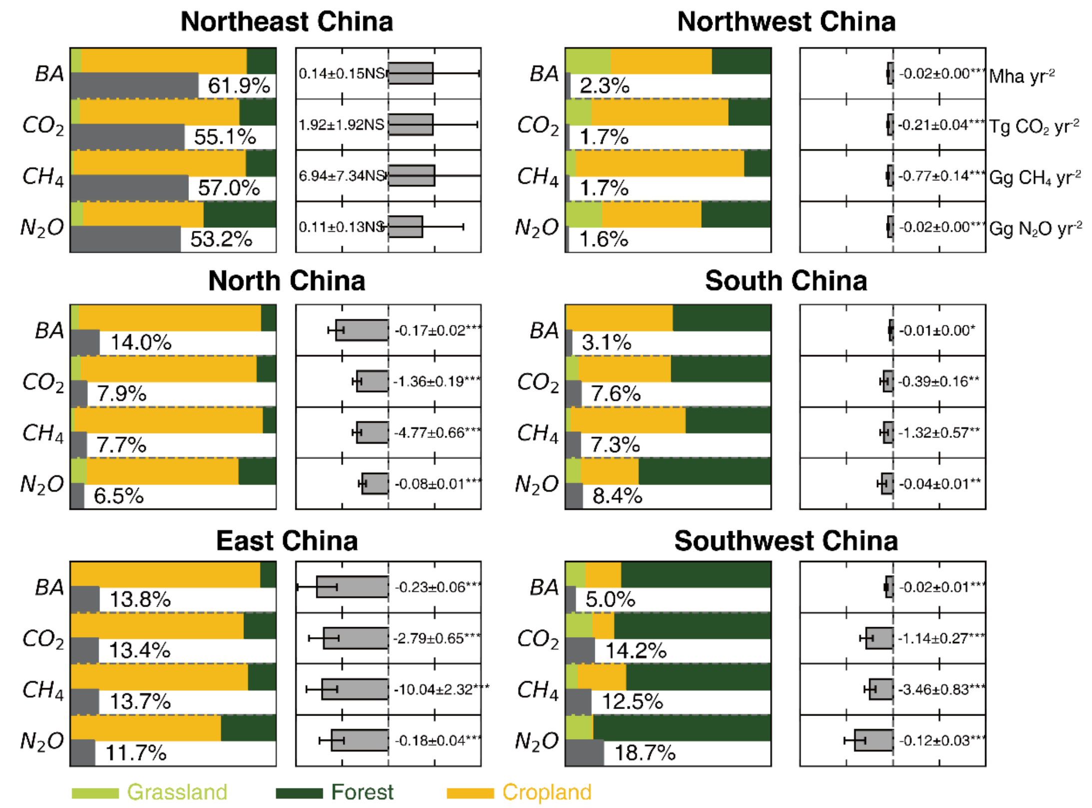

Fig. 4. Regional amounts and trends of wildfire occurrences and GHG emissions. The Y-axis of these subplots represents the four wildfire-related metrics calculated in our study: burned area, CO_2, CH_4, and N_2O emissions. The colored bars indicate the relative contributions from different land cover types within this region. The dark gray bars represent the proportions relative to the national total, with the corresponding values labeled to the left of the bars. Error bars in the right panel of each subplot depict the trends over the period from 2012 to 2022. Significant trends are denoted by asterisks (*P < 0.1, **P < 0.05, ***P<0.01; NS indicates non-significant trends).

East China is another peak region of fire activities both in terms of burned area and wildfire-induced emissions in our study. This region contains six provinces or municipalities: Anhui, Jiangsu, Zhejiang, Hunan, Hubei and Shanghai where more than

70% CO_2 wildfire emissions came from crop residue burning except for Zhejiang province. Similar to North China (Hebei, Henan, Shandong, Beijing and Tianjin), wildfire patterns in East China are featured by high intensity in agricultural-sourced fire emissions, with a total amount of more than 10 Tg wildfire emitted CO_2 and especially concentrated in the Huanghuai Plain, namely the connection area of Shandong, Henan, Jiangsu and Anhui. Altogether, these two regions have a half of the national sown area and grain production and account for 30.8% in cropland burned area, 25.4% in wildfire-induced CO_2 emissions (Fig. 4). During our study period, both of these two regions had significant declines in agricultural fires at more than -0.22 ± 0.06 Mha yr^{-2} (P<0.01) and -0.17 ± 0.02 Mha yr^{-2} (P<0.01) for East and North China, respectively. The decreasing burned area in cropland led to -2.52 ± 0.64 Tg CO_2 yr^{-2} (P<0.01), -9.17 ± 2.28 Gg CH_4 yr^{-2} (P<0.01) and 0.15 ± 0.04 Gg N_2O yr^{-2} (P<0.01) in East China. By contrast, there were an average of 0.59 Mha yr^{-1} in forest fires in the East China, three times higher than that in North China. This further contributed to significantly more wildfire-induced emission reduction, reaching 1.57 Tg CO_2, 5.03 Gg CH_4 and 0.19 Gg N_2O per year.

3.3 Comparison with other results

To assess the outcomes of this dataset, we conducted a comparative analysis by juxtaposing our estimations with those from different studies or products. Our overall emissions estimates demonstrate moderate values where the amount attributed to agricultural fires was notably lower compared to former estimates. On average, the quantities reported in regional to national scale studies were at least three times higher than our results (Hong et al., 2023; Li et al., 2022; Wu et al., 2018). These studies employed CYBA as aforementioned that the estimates of burned crop residues is calculated by the multiplying the crop production derived from statistical data, the grain-to-straw ratio from field-based analysis, and the proportion of crop residues burned in the field using empirical summaries. Previous studies had found that the use of very high residue burning ratios could be the reason for overestimates when compared with results based on categorized cropland maps (Zhang et al., 2020). Directly utilizing active fire pixels as proxies for the effects of fire activities can lead to higher values, thereby contributing to an increase in emission estimates. To address this, we employed an advanced satellite active fire dataset as a crucial supplementary observation. This dataset allowed us to refine burned area estimates by reconstructing external burned regions outside the original burned area data. We achieved this by using circular kernels centered at active fire records, aligning with the national wildfire dynamics, which are dominated by agricultural or small-sized fires. Two independent active fire products and MCD64 burned area products were incorporated as baseline to make intercomparison (Fig. 5). The sum of pixel area from MOD14 and VIIRS S-NPP active fire products was translated to 6.77 ± 1.60 Mha and 8.20 ± 2.07 Mha per year (Giglio et al., 2018, p.6; Schroeder et al., 2014). As a result, the burned area calculation by directly counting all active fire pixels was at least 27.5% higher than our results.

Expanding to a broader scope, various global fire emission inventories have been developed using different model settings. We selected four widely used products: (1)

Global Fire Emissions Database (GFED version 4.1s with small fire boosting) (van der Werf et al., 2017), (2) Fire Inventory from NCAR (FINN version 2.5) (Wiedinmyer et al., 2023), (3) Global Fire Assimilation System (GFAS version 1.2) (Kaiser et al., 2012) and (4) Quick Fire Emissions Dataset (QFED version 2.5) (Koster et al., 2015). They employ either burned area-based approaches (GFED and FINN) or fire energy-based approaches (QFED and GFAS). Our results maintain similar ranges with other global products (Fig. 5). The refined calculation for burned area estimates yielded higher values than the sole use of burned area products and lower values than those only consisting of active fire products (see details in Methods). Correspondingly, the GHGs emissions were different as well when active fire-dominated product FINN had higher estimates than ours. GFED demonstrated 64.3% to 90.3% of the results from ChinaWED in three GHGs emissions.

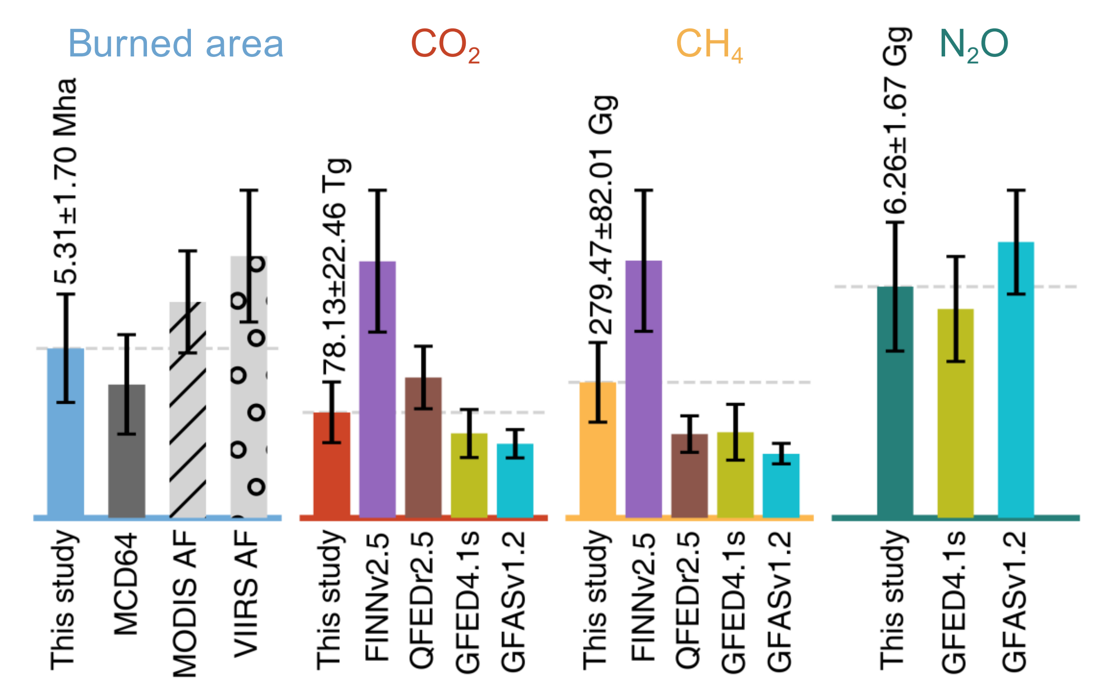

Fig. 5. Comparisons with global fire emission products as well as the burned area baseline calculation with the direct use of satellite datasets. The categories and the products are marked in their titles and x-axis.

4. Discussions

4.1 Influencing factors of the changes in wildfire seasonal cycles

In China, regulations and policies substantially impact anthropogenic activities and thus the spatiotemporal distribution of the occurrences of wildfires and emissions. In the agricultural department, the policies have addressed on the issues of straw burning due to its extensive aerosols and greenhouse gases emissions. In the early 21st century, a specific law for prevention of air pollution was published, followed by the releases of regulations on comprehensive utilization of straw (Wu et al., 2018; Zhang et al., 2015). The national-scale “Air Pollution Prevention and Control Action Plan” was initiated in 2013, with regional amendment progressively pushing from “legitimate burning" policy to "strict prohibition" (Geng et al., 2021). Since the enactment of stricter regulations on straw burning under the framework of the second revision of the Atmospheric Pollution Prevention and Control Law in 2016, significant progress has been made in controlling agricultural fires. Comprehensive control measures, especially in the agricultural sector, have substantially contributed to a rapid decline in the estimated burned area at the national scale. Between 2012 and 2016, the annual burned area decreased dramatically from 6.46 Mha yr^{-1} before 2016 to 3.89 Mha yr^{-1} after 2016. Another consequential effect of the implementation of these banning policies has been the shifts in burning seasons (Ding et al., 2019; Zhang et al., 2020). Despite Northeast China being the only region with trends contrary to the national declines, a shift in the primary burning season from autumn to spring was also observed in this area after 2013 due to the implementation of straw burning bans (Cheng et al., 2022; WANG et al., 2020).

It has been reported that there has been a noticeable decline in the global burned area driven by the expansion and intensified capital management in agricultural land use (Andela et al., 2017). Since the beginning of the 21st century, there has also been a growing emphasis on fire management within both administrative bodies and scientific communities in China. This evolution has contributed to a more stringent implementation, particularly in controlling ignition sources in agricultural practices and forest and grassland areas. From local fire suppression measures to national ignition-proof initiatives, efforts have been progressively employed to bring forest fires under control (Chen et al., 2019; Ying et al., 2018). In comparison with forest fire dynamics reported in previous studies focusing on the first decade of this century, the southern part of China experienced a significant decline in burned area as well as wildfire-induced emissions (Wang et al., 2023b; Ying et al., 2018; Zong et al., 2022). Whilst the establishment and improvement of legal systems and infrastructure for forest and grassland fire prevention, dealing with uncontrolled transboundary fires remains challenging. Nationally, an area of 0.07 Mha yr^{-1} was affected within the 10 km buffer zone near the borders with neighboring countries. This accounted for 1.3% of domestic burned area and contributed to 1.03 Tg yr^{-1} of CO_2, 3.35 Gg yr^{-1} of CH_4, and 0.09 Gg yr^{-1} of N_2O.

4.2 Improvements of ChinaWED to previous studies

As described in the aforementioned texts, we refined our estimates of emission factors, fuel loadings and burned area mainly with a set of more localized parameters and advanced satellite-based observations. Fuel loadings in these previous global products are mainly derived from biogeochemical models in these global products. According to the recent studies, the use of aboveground biomass (AGB) as a proxy of fuel loadings can enable indirect estimations of dry matter and improve fire emission estimates (Di Giuseppe et al., 2021). We thus used a high-resolution harmonized carbon density map that was consistently and seamlessly reported across a wide range of vegetation types based on the relative spatial extent of each type. Emission factor is a scalar that evaluate the ratio between emission and the total amount of dry matter that was consumed during burning processes. In this study in addition to the previously summarized emission factors, we collected the field-based research in China and neighboring countries and recompiled the values into the new table of wildfire emission factors for different land cover types. A detailed selection of these components can be found in Table S2. Although the use of AGB as a fuel load proxy has demonstrated superior performance compared to vegetation models or FRP-derived estimations (Di Giuseppe et al., 2021), it is crucial to highlight that our current model relies entirely on a static AGB dataset. This limitation creates a scenario where fuel loads have few impacts on the variability of emission estimates. Future improvements could be achieved by integrating dynamic input products and enhancing the precision of AGB estimations in croplands.

Additionally in the estimates of burned area, ChinaWED leveraged the sensitivity of active fire products with higher spatial resolution and developed a new set of calculation methods that were suitable for smaller fires. The global products had different frameworks where FINN focuses on active fire detection clusters joined for the determination of extended burned areas and the burned area from GFED is mainly derived based on a linear combination of the distribution of active fire and original burned area data. QFED and GFAS utilize fire energy as the intermediate product to represent the effects of fires for estimating wildfire-induced emissions. These models employ empirical continuous functions to incorporate discrete observations and calculate the temporal integral of fire radiative power (FRP). Furthermore, ChinaWED is designed for the analysis of wildfire-induced GHG emissions. Most products reported wildfire-induced CO_2 and CH_4 emissions while only two of them provided N_2O emission estimates (Fig. 5).

Code and data availability

Python code for this model can be obtained from https://zenodo.org/records/13800556 (python version 3.11.6). Key packages used in the code include rasterio (version 1.3.9), numpy (version 1.25.2), pandas (version 2.1.3) and scipy (version 1.10.1). Fire products include MCD64A1.061 (doi.org/10.5067/MODIS/MCD64A1.061) and VIIRS S-NPP active fire (doi.org/10.1016/j.rse.2013.12.008). Aboveground biomass data is available from doi.org/10.1038/s41597-020-0444-4. Different crop types are available from double season paddy rice (doi.org/10.3390/rs13224609), single season rice (doi.org/10.57760/sciencedb.06963), maize (doi:10.6084/m9.figshare.17091653), winter wheat (doi.org/10.6084/m9.figshare.12003990) and sugarcane (doi.org/10.3390/rs14051274), respectively.

5. Conclusions

Wildfire is one of the most common land-surface disturbances to ecological and socioeconomical processes. It combusts vegetation and releases greenhouse gases and aerosols. Employing the burned area-based approach, we featured multisource fire locations, updated emission factors, and high-resolution fuel load maps to generate a new China wildfire emission dataset. The wildfire dynamics showed that during the past decade, an average of 5.31 ± 1.70 Mha burned area, 78.13 ± 22.46 Tg CO_2, 279.47 ± 82.01 Gg CH_4, and 6.26 ± 1.67 Gg N_2O per year was observed. At the national scale, the spatiotemporal characteristics of fire occurrences were markedly influenced by agricultural activities, which contributed to more than four-fifths in area and at least half in greenhouse gas emissions. The extensive agricultural fires played an important role in shaping the seasonal cycle of wildfire emissions (Hong et al., 2023; Xu et al., 2023). Northeast, North, and East China emerged as hotspots for this type of fires, with the major peak of emissions occurring in mid-spring to early-summer. We observed rapid and significant decline of burned area and wildfire-induced emissions in vast areas in China that may be largely attributed to the implementation of fire prevention and bans on straw burning. Notably, the relative decline rate of burned, translating to around 5.8% per year, was four times higher than the global average (Andela et al., 2017). Northeast China was the only region with an opposite trend, suggesting a situation that requires more adaptive policies rather than mandatory bans. Compared with estimations by other studies and global products, our results have moderate values where the mismatches in burned area and estimates of burned crop residues contributed largely. Overall, the calculation of burned area for small-sized fire activities and the recalibrated emission factors, tailored for wildfires in China, contribute to the findings of this study. These results offer new insights into the spatiotemporal patterns of China's wildfire-induced greenhouse gas emissions and provide important estimates as a part of the budget for the national terrestrial ecosystems. Future updates will focus on integrating additional field-based studies and refining the estimates of various burning processes.

Author contribution

Z.L. and X.W. designed the experiments and Z.L. carried them out. Z.L. developed the model code and performed the calculation. Z.L., L.H. and X.W. validated the results. Z.L. prepared the manuscript with contributions from all co-authors.

Competing interests

The contact author has declared that none of the authors has any competing interests

Reference

Andela, N., Morton, D. C., Giglio, L., Chen, Y., van der Werf, G. R., Kasibhatla, P. S., DeFries, R. S., Collatz, G. J., Hantson, S., Kloster, S., Bachelet, D., Forrest, M., Lasslop, G., Li, F., Mangeon, S., Melton, J. R., Yue, C., and Randerson, J. T.: A human-driven decline in global burned area, Science, 356, 1356–1362, https://doi.org/10.1126/science.aal4108, 2017.

Bauters, M., Drake, T. W., Wagner, S., Baumgartner, S., Makelele, I. A., Bode, S., Verheyen, K., Verbeeck, H., Ewango, C., Cizungu, L., Van Oost, K., and Boeckx, P.: Fire-derived phosphorus fertilization of African tropical forests, Nature Communications, 12, 5129, https://doi.org/10.1038/s41467-021-25428-3, 2021.

Beck, H. E., Zimmermann, N. E., McVicar, T. R., Vergopolan, N., Berg, A., and Wood, E. F.: Present and future Köppen-Geiger climate classification maps at 1-km resolution, Scientific Data, 5, 180214, https://doi.org/10.1038/sdata.2018.214, 2018.

Chen, A., Tang, R., Mao, J., Yue, C., Li, X., Gao, M., Shi, X., Jin, M., Ricciuto, D., Rabin, S., Ciais, P., and Piao, S.: Spatiotemporal dynamics of ecosystem fires and biomass burning-induced carbon emissions in China over the past two decades, Geography and Sustainability, 1, 47–58, https://doi.org/10.1016/j.geosus.2020.03.002, 2020.

Chen, C., Park, T., Wang, X., Piao, S., Xu, B., Chaturvedi, R. K., Fuchs, R., Brovkin, V., Ciais, P., Fensholt, R., Tommervik, H., Bala, G., Zhu, Z., Nemani, R. R., and Myneni, R. B.: China and India lead in greening of the world through land-use management, Nature Sustainability, 2, 122–129, https://doi.org/10.1038/s41893-019-0220-7, 2019.

Cheng, Y., Cao, X., Liu, J., Yu, Q., Zhong, Y., Geng, G., Zhang, Q., and He, K.: New open burning policy reshaped the aerosol characteristics of agricultural fire episodes in Northeast China, Science of The Total Environment, 810, 152272, https://doi.org/10.1016/j.scitotenv.2021.152272, 2022.

Cui, L., Luo, C., Yao, C., Zou, Z., Wu, G., Li, Q., and Wang, X.: The Influence of Climate Change on Forest Fires in Yunnan Province, Southwest China Detected by GRACE Satellites, Remote Sensing, 14, 712, https://doi.org/10.3390/rs14030712, 2022.

Curtis, P. G., Slay, C. M., Harris, N. L., Tyukavina, A., and Hansen, M. C.: Classifying drivers of global forest loss, Science, 361, 1108–1111, https://doi.org/10.1126/science.aau3445, 2018.

Di Giuseppe, F., Benedetti, A., Coughlan, R., Vitolo, C., and Vuckovic, M.: A Global Bottom-Up Approach to Estimate Fuel Consumed by Fires Using Above Ground Biomass Observations, Geophys. Res. Lett., 48, e2021GL095452, https://doi.org/10.1029/2021gl095452, 2021.

Ding, A., Huang, X., Nie, W., Chi, X., Xu, Z., Zheng, L., Xu, Z., Xie, Y., Qi, X., Shen, Y., Sun, P., Wang, J., Wang, L., Sun, J., Yang, X.-Q., Qin, W., Zhang, X., Cheng, W., Liu, W., Pan, L., and Fu, C.: Significant reduction of PM2.5 in eastern china due to regional-scale emission control: evidence from SORPES in 2011–2018, Atmospheric Chemistry and Physics, 19, 11791–11801, https://doi.org/10.5194/acp-19-11791-2019, 2019.

Dong, J., Fu, Y., Wang, J., Tian, H., Fu, S., Niu, Z., Han, W., Zheng, Y., Huang, J., and Yuan, W.: Early-season mapping of winter wheat in China based on Landsat and Sentinel images, Earth Syst. Sci. Data, 12, 3081–3095, https://doi.org/10.5194/essd-12-3081-2020, 2020.

Friedlingstein, P., O'Sullivan, M., Jones, M. W., Andrew, R. M., Gregor, L., Hauck, J., Le Quéré, C., Luijkx, I. T., Olsen, A., Peters, G. P., Peters, W., Pongratz, J., Schwingshackl, C., Sitch, S., Canadell, J. G., Ciais, P., Jackson, R. B., Alin, S. R., Alkama, R., Arneth, A., Arora, V. K., Bates, N. R., Becker, M., Bellouin, N., Bittig, H. C., Bopp, L., Chevallier, F., Chini, L. P., Cronin, M., Evans, W., Falk, S., Feely, R. A., Gasser, T., Gehlen, M., Gkritzalis, T., Gloege, L., Grassi, G., Gruber, N., Gürses, Ö., Harris, I., Hefner, M., Houghton, R. A., Hurtt, G. C., Iida, Y., Ilyina, T., Jain, A. K., Jersild, A., Kadono, K., Kato, E., Kennedy, D., Klein Goldewijk, K., Knauer, J., Korsbakken, J. I., Landschützer, P., Lefèvre, N., Lindsay, K., Liu, J., Liu, Z., Marland, G., Mayot, N., McGrath, M. J., Metzl, N., Monacci, N. M., Munro, D. R., Nakaoka, S.-I., Niwa, Y., O'Brien, K., Ono, T., Palmer, P. I., Pan, N., Pierrot, D., Pocock, K., Poulter, B., Resplandy, L., Robertson, E., Rödenbeck, C., Rodriguez, C., Rosan, T. M., Schwinger, J., Séférian, R., Shutler, J. D., Skjelvan, I., Steinhoff, T., Sun, Q., Sutton, A. J., Sweeney, C., Takao, S., Tanhua, T., Tans, P. P., Tian, X., Tian, H., Tilbrook, B., Tsujino, H., Tubiello, F., van der Werf, G. R., Walker, A. P., Wanninkhof, R., Whitehead, C., Willstrand Wranne, A., et al.: Global Carbon Budget 2022, Earth System Science Data, 14, 4811–4900, https://doi.org/10.5194/essd-14-4811-2022, 2022.

Geng, G., Zheng, Y., Zhang, Q., Xue, T., Zhao, H., Tong, D., Zheng, B., Li, M., Liu, F., Hong, C., He, K., and Davis, S. J.: Drivers of PM2.5 air pollution deaths in China 2002–2017, Nature Geoscience, 14, 645–650, https://doi.org/10.1038/s41561-021-00792-3, 2021.

Giglio, L., Boschetti, L., Roy, D. P., Humber, M. L., and Justice, C. O.: The Collection 6 MODIS burned area mapping algorithm and product, Remote Sensing of Environment, 217, 72–85, https://doi.org/10.1016/j.rse.2018.08.005, 2018.

Guo, J., Feng, H., Peng, C., Du, J., Wang, W., Kneeshaw, D., Pan, C., Roberge, G., Feng, L., and Chen, A.: Fire effects on soil CH4 and N2O fluxes across terrestrial ecosystems, Science of The Total Environment, 948, 174708, https://doi.org/10.1016/j.scitotenv.2024.174708, 2024.

Hong, X., Zhang, C., Tian, Y., Wu, H., Zhu, Y., and Liu, C.: Quantification and evaluation of atmospheric emissions from crop residue burning constrained by satellite observations in China during 2016–2020, Science of The Total Environment, 865, 161237, https://doi.org/10.1016/j.scitotenv.2022.161237, 2023.

Kaiser, J. W., Heil, A., Andreae, M. O., Benedetti, A., Chubarova, N., Jones, L., Morcrette, J. J., Razinger, M., Schultz, M. G., Suttie, M., and van der Werf, G. R.: Biomass burning emissions estimated with a global fire assimilation system based on observed fire radiative power, Biogeosciences, 9, 527–554, https://doi.org/10.5194/bg-9-527-2012, 2012.

Koster, R. D., Darmenov, A. S., and da Silva, A. M.: The Quick Fire Emissions Dataset (QFED): Documentation of Versions 2.1, 2.2 and 2.4, 2015.

Li, J., Li, Y., Bo, Y., and Xie, S.: High-resolution historical emission inventories of crop residue burning in fields in China for the period 1990–2013, Atmospheric Environment, 138, 152–161, https://doi.org/10.1016/j.atmosenv.2016.05.002, 2016.

Li, R., He, X., Wang, H., Wang, Y., Zhang, M., Mei, X., Zhang, F., and Chen, L.: Estimating Emissions from Crop Residue Open Burning in Central China from 2012 to 2020 Using Statistical Models Combined with Satellite Observations, Remote Sensing, 14, 3682, https://doi.org/10.3390/rs14153682, 2022.

Li, W., MacBean, N., Ciais, P., Defourny, P., Lamarche, C., Bontemps, S., Houghton, R. A., and Peng, S.: Gross and net land cover changes in the main plant functional types derived from the annual ESA CCI land cover maps (1992–2015), Earth System Science Data, 10, 219–234, https://doi.org/10.5194/essd-10-219-2018, 2018.

Liu, Y., Hu, C., Zhan, W., Sun, C., Murch, B., and Ma, L.: Identifying industrial heat sources using time-series of the VIIRS Nightfire product with an object-oriented approach, Remote Sensing of Environment, 204, 347–365, https://doi.org/10.1016/j.rse.2017.10.019, 2018.

Liu, Z., Deng, Z., He, G., Wang, H., Zhang, X., Lin, J., Qi, Y., and Liang, X.: Challenges and opportunities for carbon neutrality in China, Nat Rev Earth Environ, 3, 141–155, https://doi.org/10.1038/s43017-021-00244-x, 2022.

Noon, M. L., Goldstein, A., Ledezma, J. C., Roehrdanz, P. R., Cook-Patton, S. C., Spawn-Lee, S. A., Wright, T. M., Gonzalez-Roglich, M., Hole, D. G., Rockström, J., and Turner, W. R.: Mapping the irrecoverable carbon in Earth’s ecosystems, Nature Sustainability, 5, 37–46, https://doi.org/10.1038/s41893-021-00803-6, 2022.

Page, S., Mishra, S., Agus, F., Anshari, G., Dargie, G., Evers, S., Jauhiainen, J., Jaya, A., Jovani-Sancho, A. J., Laurén, A., Sjögersten, S., Suspense, I. A., Wijedasa, L. S., and Evans, C. D.: Anthropogenic impacts on lowland tropical peatland biogeochemistry, Nature Reviews Earth & Environment, 3, 426–443, https://doi.org/10.1038/s43017-022-00289-6, 2022.

Pan, B., Zheng, Y., Shen, R., Ye, T., Zhao, W., Dong, J., Ma, H., and Yuan, W.:

High Resolution Distribution Dataset of Double-Season Paddy Rice in China, Remote Sensing, 13, 4609, https://doi.org/10.3390/rs13224609, 2021.

Rodríguez Vásquez, M. J., Benoist, A., Roda, J.-M., and Fortin, M.: Estimating Greenhouse Gas Emissions From Peat Combustion in Wildfires on Indonesian Peatlands, and Their Uncertainty, Global Biogeochemical Cycles, 35, e2019GB006218, https://doi.org/10.1029/2019GB006218, 2021.

Schroeder, W., Oliva, P., Giglio, L., and Csiszar, I. A.: The New VIIRS 375 m active fire detection data product: Algorithm description and initial assessment, Remote Sensing of Environment, 143, 85–96, https://doi.org/10.1016/j.rse.2013.12.008, 2014.

Shen, R., Dong, J., Yuan, W., Han, W., Ye, T., and Zhao, W.: A 30 m Resolution Distribution Map of Maize for China Based on Landsat and Sentinel Images, Journal of Remote Sensing, 2022, https://doi.org/10.34133/2022/9846712, 2022.

Shen, R., Pan, B., Peng, Q., Dong, J., Chen, X., Zhang, X., Ye, T., Huang, J., and Yuan, W.: High-resolution distribution maps of single-season rice in China from 2017 to 2022, Earth Syst. Sci. Data, 15, 3203–3222, https://doi.org/10.5194/essd-15-3203-2023, 2023.

Spawn, S. A., Sullivan, C. C., Lark, T. J., and Gibbs, H. K.: Harmonized global maps of above and belowground biomass carbon density in the year 2010, Sci Data, 7, 112, https://doi.org/10.1038/s41597-020-0444-4, 2020.

Tang, X., Zhao, X., Bai, Y., Tang, Z., Wang, W., Zhao, Y., Wan, H., Xie, Z., Shi, X., Wu, B., Wang, G., Yan, J., Ma, K., Du, S., Li, S., Han, S., Ma, Y., Hu, H., He, N., Yang, Y., Han, W., He, H., Yu, G., Fang, J., and Zhou, G.: Carbon pools in China's terrestrial ecosystems: New estimates based on an intensive field survey, Proceedings of the National Academy of Sciences, 115, 4021–4026, https://doi.org/10.1073/pnas.1700291115, 2018.

Vernooij, R., Giongo, M., Borges, M. A., Costa, M. M., Barradas, A. C. S., and Van Der Werf, G. R.: Intraseasonal variability of greenhouse gas emission factors from biomass burning in the Brazilian Cerrado, Biogeosciences, 18, 1375–1393, https://doi.org/10.5194/bg-18-1375-2021, 2021.

WANG, L., JIN, X., WANG, Q., MAO, H., LIU, Q., WENG, G., and WANG, Y.: Spatial and temporal variability of open biomass burning in Northeast China from 2003 to 2017, Atmospheric and Oceanic Science Letters, 13, 240–247, https://doi.org/10.1080/16742834.2020.1742574, 2020.

Wang, S., Zhang, H., Feng, Z., Wang, Y., Su, J., Gao, K., and Li, J.: Dispersal Limitation Dominates the Spatial Distribution of Forest Fuel Loads in Chongqing, China, Ecosystem Health and Sustainability, 9, 0079, https://doi.org/10.34133/ehs.0079, 2023a.

Wang, Z., Huang, R., Yao, Q., Zong, X., Tian, X., Zheng, B., and Trouet, V.: Strong winds drive grassland fires in China, Environ. Res. Lett., 18, 015005, https://doi.org/10.1088/1748-9326/aca921, 2023b.

van Wees, D., van der Werf, G. R., Randerson, J. T., Rogers, B. M., Chen, Y., Veraverbeke, S., Giglio, L., and Morton, D. C.: Global biomass burning fuel consumption and emissions at 500 m spatial resolution based on the Global Fire Emissions Database (GFED), Geoscientific Model Development, 15, 8411–8437, https://doi.org/10.5194/gmd-15-8411-2022, 2022.

van der Werf, G. R., Randerson, J. T., Giglio, L., van Leeuwen, T. T., Chen, Y., Rogers, B. M., Mu, M., van Marle, M. J. E., Morton, D. C., Collatz, G. J., Yokelson, R. J., and Kasibhatla, P. S.: Global fire emissions estimates during 1997-2016, Earth Syst. Sci. Data, 9, 697–720, https://doi.org/10.5194/essd-9-697-2017, 2017.

Wiedinmyer, C., Kimura, Y., McDonald-Buller, E. C., Emmons, L. K., Buchholz, R. R., Tang, W., Seto, K., Joseph, M. B., Barsanti, K. C., Carlton, A. G., and Yokelson, R.: The Fire Inventory from NCAR version 2.5: an updated global fire emissions model for climate and chemistry applications, EGUsphere, 1–45, https://doi.org/10.5194/egusphere-2023-124, 2023.

Wu, H., Zhang, J., Zhang, Z., Han, J., Cao, J., Zhang, L., Luo, Y., Mei, Q., Xu, J., and Tao, F.: AsiaRiceYield4km: seasonal rice yield in Asia from 1995 to 2015, Earth System Science Data, 15, 791–808, https://doi.org/10.5194/essd-15-791-2023, 2023.

Wu, J., Kong, S., Wu, F., Cheng, Y., Zheng, S., Yan, Q., Zheng, H., Yang, G., Zheng, M., Liu, D., Zhao, D., and Qi, S.: Estimating the open biomass burning emissions in central and eastern China from 2003 to 2015 based on satellite observation, Atmospheric Chemistry and Physics, 18, 11623–11646, https://doi.org/10.5194/acp-18-11623-2018, 2018.

Xu, R., Ye, T., Yue, X., Yang, Z., Yu, W., Zhang, Y., Bell, M. L., Morawska, L., Yu, P., Zhang, Y., Wu, Y., Liu, Y., Johnston, F., Lei, Y., Abramson, M. J., Guo, Y., and Li, S.: Global population exposure to landscape fire air pollution from 2000 to 2019, Nature, 621, 521–529, https://doi.org/10.1038/s41586-023-06398-6, 2023.

Ying, L., Han, J., Du, Y., and Shen, Z.: Forest fire characteristics in China: Spatial patterns and determinants with thresholds, Forest Ecology and Management, 424, 345–354, https://doi.org/10.1016/j.foreco.2018.05.020, 2018.

Ying, L., Cheng, H., Shen, Z., Guan, P., Luo, C., and Peng, X.: Relative humidity and agricultural activities dominate wildfire ignitions in yunnan, southwest china: patterns, thresholds, and implications, Agricultural and Forest Meteorology, 307, 108540, https://doi.org/10.1016/j.agrformet.2021.108540, 2021.

Zhang, H., Ye, X., Cheng, T., Chen, J., Yang, X., Wang, L., and Zhang, R.: A laboratory study of agricultural crop residue combustion in china: emission factors and emission inventory, Atmospheric Environment, 42, 8432–8441, https://doi.org/10.1016/j.atmosenv.2008.08.015, 2008.

Zhang, H., Hu, D., Chen, J., Ye, X., Wang, S. X., Hao, J. M., Wang, L., Zhang, R., and An, Z.: Particle Size Distribution and Polycyclic Aromatic Hydrocarbons Emissions from Agricultural Crop Residue Burning, Environmental Science & Technology, 45, 5477–5482, https://doi.org/10.1021/es1037904, 2011.

Zhang, T., Wooster, M. J., Green, D. C., and Main, B.: New field-based agricultural biomass burning trace gas, PM2.5, and black carbon emission ratios and factors measured in situ at crop residue fires in eastern china, Atmospheric Environment, 121, 22–34, https://doi.org/10.1016/j.atmosenv.2015.05.010, 2015.

Zhang, T., de Jong, M. C., Wooster, M. J., Xu, W., and Wang, L.: Trends in eastern China agricultural fire emissions derived from a combination of geostationary (Himawari) and polar (VIIRS) orbiter fire radiative power products, Atmospheric Chemistry and Physics, 20, 10687–10705, https://doi.org/10.5194/acp-20-10687-2020, 2020.

Zhao, F., Liu, Y., and Shu, L.: Change in the fire season pattern from bimodal to unimodal under climate change: The case of Daxing'anling in Northeast China, Agricultural and Forest Meteorology, 291, 108075, https://doi.org/10.1016/j.agrformet.2020.108075, 2020.

Zheng, Y., Li, Z., Pan, B., Lin, S., Dong, J., Li, X., and Yuan, W.: Development of a Phenology-Based Method for Identifying Sugarcane Plantation Areas in China Using High-Resolution Satellite Datasets, Remote Sensing, 14, 1274, https://doi.org/10.3390/rs14051274, 2022.

Zong, X., Tian, X., Yao, Q., Brown, P. M., Zong, X., Tian, X., Yao, Q., and Brown, P. M.: An analysis of fatalities from forest fires in China, 1951–2018, Int. J. Wildland Fire, 31, 507–517, https://doi.org/10.1071/WF21137, 2022.